



저작자표시-비영리-변경금지 2.0 대한민국

이용자는 아래의 조건을 따르는 경우에 한하여 자유롭게

- 이 저작물을 복제, 배포, 전송, 전시, 공연 및 방송할 수 있습니다.

다음과 같은 조건을 따라야 합니다:



저작자표시. 귀하는 원저작자를 표시하여야 합니다.



비영리. 귀하는 이 저작물을 영리 목적으로 이용할 수 없습니다.



변경금지. 귀하는 이 저작물을 개작, 변형 또는 가공할 수 없습니다.

- 귀하는, 이 저작물의 재이용이나 배포의 경우, 이 저작물에 적용된 이용허락조건을 명확하게 나타내어야 합니다.
- 저작권자로부터 별도의 허가를 받으면 이러한 조건들은 적용되지 않습니다.

저작권법에 따른 이용자의 권리는 위의 내용에 의하여 영향을 받지 않습니다.

이것은 [이용허락규약\(Legal Code\)](#)을 이해하기 쉽게 요약한 것입니다.

[Disclaimer](#)

Master's Thesis

DFT Studies on Van der Waals Multiferroicity
and Perovskite Solar Cell

EUN MI KIM

Department of Chemistry

Graduate School of UNIST

2019

DFT Studies on Van der Waals Multiferroicity and Perovskite Solar Cell

EUN MI KIM

Department of Chemistry

Graduate School of UNIST

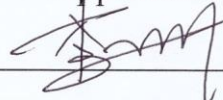
DFT Studies on Van der Waals Multiferroicity and Perovskite Solar Cell

A thesis
submitted to the Graduate School of UNIST
in partial fulfillment of the
requirements for the degree of
Master of Science

EUN MI KIM

06. 07. 2019

Approved by



Advisor

Geunsik Lee

DFT Studies on Van der Waals Multiferroicity and Perovskite Solar Cell

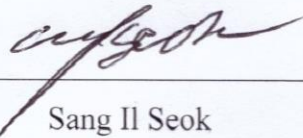
EUN MI KIM

This certifies that the thesis/dissertation of EUN MI KIM is approved.

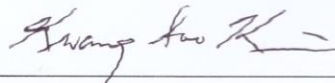
06. 07. 2019



Advisor: Geunsik Lee



Sang Il Seok



Kwang Soo Kim

Abstract

The DFT (Density Functional Theory) method has been a powerful tool to investigate the electronic structures of molecules and atoms, especially been very useful in solid state physics. Here, the DFT method has been applied to study two interesting topics; Van der Waals Multiferroicity and Perovskite Solar cell.

Materials that are simultaneously ferromagnetic and ferroelectric – multiferroics – promise the control of disparate ferroic orders, leading to technological advances in microwave magnetoelectric applications and next generation of spintronics. Single-phase multiferroics are challenged by the opposite *d*-orbital occupations imposed by the two ferroics, and heterogeneous nanocomposite multiferroics demand ingredients' structural compatibility with the resultant multiferroicity exclusively at inter-materials boundaries. Here, we propose the two-dimensional heterostructure multiferroics by stacking up atomic layers of ferromagnetic Cr₂Ge₂Te₆ and ferroelectric In₂Se₃, thereby leading to all-atomic multiferroicity. Through first-principles density functional theory calculations, we find as In₂Se₃ reverses its polarization, the magnetism of Cr₂Ge₂Te₆ is switched, and correspondingly In₂Se₃ becomes a switchable magnetic semiconductor due to proximity effect. This unprecedented multiferroic duality (i.e., switchable ferromagnet and switchable magnetic semiconductor) enables both layers for logic applications. Van der Waals heterostructure multiferroics open the door for exploring the low-dimensional magnetoelectric physics and spintronic applications based on artificial superlattices.

In hybrid organic-inorganic halide perovskite solar cells, organic graphene nanoribbons (GNRs) can be a good candidate as carrier extraction interlayers owing to the capability of tuning the band edge energy levels through varying the size of width and the type of edge functionalization. Here, by using the density function theory (DFT) method, the electronic structures of H or F edge functionalized armchair type GNRs on MAPbI₃(001) are calculated. It is shown that the H/F-passivated GNR with width of seven carbon atoms exhibits a good band alignment for hole/electron extraction. Exploiting the unzipping synthesis of carbon nanotubes in the solution phase, our result provides a facial strategy for efficient carrier extraction.

Contents

I. Multiferroicity in atomic Van der Waals heterostructures	
I.1 Introduction	9
I.2 Computational Method	10
I.3 Result and Discussion	11
I.4 Conclusion	19
I.5 References	19
II. Edge Functionalized Graphene Nanoribbons with tunable band alignments for Carrier Transport Interlayer in Organic-Inorganic Perovskite Solar Cells	
II.1 Introduction	22
II.2 Computational Method	23
II.3 Result and Discussion	25
II.4 Conclusion	28
II.5 References	29

List of Figures

- Figure 1** Van der Waals $\text{Cr}_2\text{Ge}_2\text{Te}_6/\text{In}_2\text{Se}_3$ heterostructure and magnetoelectric coupling.
- Figure 2** Spin-polarized and Cr d orbital-decomposed band structures of $\text{Cr}_2\text{Ge}_2\text{Te}_6/\text{In}_2\text{Se}_3$ heterostructures
- Figure 3** Calculated magnetocrystalline anisotropy of $\text{Cr}_2\text{Ge}_2\text{Te}_6$ in the heterostructure versus the vdW (Van der Waals) interlayer distance
- Figure 4** Magnetoelectric effect in In_2Se_3 , mediated by the magnetic proximity to $\text{Cr}_2\text{Ge}_2\text{Te}_6$.
- Figure 5** Structures of MAPbI_3 (I_4/mcm), H-GNR, F-GNR and Clean $\text{MAPbI}_3(001)$
- Figure 6** Band structures of MAPbI_3 , H-GNR and F-GNR
- Figure 7** Band alignments of H-GNR and F-GNR
- Figure 8** Optimized structure, Band structure and Density Of States of H-GNR/ MAPbI_3
- Figure 9** Optimized structure, Band structure and Density Of States of F-GNR/ MAPbI_3

I. Multiferroicity in atomic Van der Waals heterostructures

I.1 Introduction

Multiferroics, a class of functional materials that simultaneously possess more than one ferroic orders such as ferromagnetism and ferroelectricity, hold great promise in magnetoelectric applications due to the inherent coupling between ferroic orders,¹⁻⁶ leading to technological advances in next generation of spintronics and microwave magnetoelectric devices. However, single-phase multiferroics are challenged by the different ferroics' contradictory preference on the *d*-orbital occupation of metal ions: ferroelectricity arising from off-center cations requires empty *d*-orbitals, whereas ferromagnetism usually results from partially filled *d*-orbitals.⁷ Conventional perovskite multiferroics (chemical formula: ABO_3) have lone-pair-active A-sites which move to off-centers of centrosymmetric crystals for electric polarization, and B-sites with unpaired electrons for magnetic order. Because the ferroelectric and magnetic order in these materials are associated with different ions, the coupling between the ferroic orders are usually weak.

Heterogeneous multiferroics, synthesized composites of two mixed phases,⁸ have the coupling between ferroelectric and magnetic order exclusively at inter-materials boundaries, with magnetoelectric effects occasionally established via interfacial magnetoelastic effect. As an example, magnetic nanopillars could be embedded in ferroelectric matrix. However, these heterogeneous multiferroics stringently demand the constituent materials on their structural similarity, lattice match and chemical compatibility, and have weak magnetoelectric effects limited by the interface/bulk ratios.

Van der Waals (vdW) crystals emerged as ideal material systems with unprecedented freedom for heterostructure construction.⁹ Recent experimental advance discovered ferromagnetism^{10,11,12} and ferroelectricity¹³ in different two-dimensional vdW crystals separately. It remains a paramount challenge to realize multiple ferroic orders in a single-phase 2D material simultaneously,¹⁴⁻¹⁷ as each order encounters its own challenge (e.g., ferromagnetism in 2D systems suffers from enhanced thermal fluctuations, whereas ferroelectricity the depolarization field). Constructing heterostructures of 2D magnets and 2D ferroelectrics potentially provides a generally applicable route to create 2D multiferroics. However, the fundamental question remains regarding whether the interlayer magnetoelectric coupling can be established, given the presence of the interlayer vdW spacing. If realized, layered heterostructure multiferroics would provide completely new platforms with all atoms participating in the inter-ferroics coupling, and largely reshape the landscape of multiferroics based on vdW superlattices.

Through first-principles density functional theory (DFT) calculations based on a bilayer heterostructure of ferromagnetic $\text{Cr}_2\text{Ge}_2\text{Te}_6$ and ferroelectric In_2Se_3 monolayers,¹⁸⁻²¹ we discovered a strong interlayer magnetoelectric effect: the reversal electric polarizations in In_2Se_3 switches the magnetocrystalline anisotropy of $\text{Cr}_2\text{Ge}_2\text{Te}_6$ between out-of-plane and in-plane orientations. For a 2D ferromagnet, such a change in magnetic anisotropy corresponds to a switching on/off of the ferromagnetic order at finite temperatures, for easy-axis anisotropy opens spin wave excitation gap and thus suppresses the thermal fluctuations, but easy-plane anisotropy does not.^{10,22,23} The switching of ferromagnetic order by electric polarization promises a novel design of magnetic memory. Detailed analysis unraveled the interfacial hybridization as the cause of interlayer magnetoelectric coupling. Furthermore, In_2Se_3 becomes magnetized due to the proximity to $\text{Cr}_2\text{Ge}_2\text{Te}_6$, making In_2Se_3 a single-phase multiferroics (i.e., ferromagnetic and ferroelectric orders coexist in In_2Se_3), although apparently the magnetization of In_2Se_3 requires the presence of the adjacent $\text{Cr}_2\text{Ge}_2\text{Te}_6$. Such multiferroicity duality - that is, the interlayer multiferroicity and the In_2Se_3 intralayer multiferroicity - provides unique solid-state system in which ferroelectric and ferromagnetic orders interplay inherently. This unusual multiferroicity duality in vdW heterostructures may open avenues for developing new concepts of magnetoelectric devices: using single knob (the orientation of electric polarization in In_2Se_3) to control the magnetic order in both In_2Se_3 and $\text{Cr}_2\text{Ge}_2\text{Te}_6$. We envision the multiferroicity duality potentially enriches the freedom of layer-resolved data storage and that of information processing due to the diverse magnetoelectric and magneto-optic properties of constituent layers.

I.2 Computational Method

The DFT method and parameters. All the calculations were performed by the DFT method implemented in Vienna *ab initio* Simulation Package (VASP),³⁴ with the Perdew-Burke-Ernzerhof (PBE) functional³⁵ in the scheme of generalized gradient approximation (GGA). The main data was calculated by GGA + U based on the Liechtenstein approach with $U = 0.5$ eV and $J = 0.0$ eV. The van der Waals interatomic forces are described by the D2 Grimme method.³⁶ The K-mesh of $6 \times 6 \times 1$ and the energy cutoff of 300 eV are used for the structural optimization. The dipole correction is included to exclude spurious dipole-dipole interaction between periodic images.

I.3 Result and Discussion

In this work, the lattice constant of $\text{Cr}_2\text{Ge}_2\text{Te}_6$ adopted the experimental value 6.83 \AA and was fixed in heterostructures for the sake of minimizing artifact effects, considering the magnetic properties of 2D $\text{Cr}_2\text{Ge}_2\text{Te}_6$ are sensitive to structure parameters. It has been reported that a monolayer In_2Se_3 of either zincblende or wurtzite stacking is unstable with a tendency of the lateral displacement of the top Se layer, leading to the energetically degenerate ferroelectric monolayer.¹⁸ Although the one relaxed from the zincblende stacking is chosen in this study, it will be also applicable to the other derived from the wurtzite, because the main mechanism to be shown is determined by the interfacial monolayers and thus independent of the detailed stacking type of the multilayer In_2Se_3 . The optimized lattice constant of 1×1 - In_2Se_3 (4.106 \AA), is strained by -4.0% to match In_2Se_3 - $\sqrt{3} \times \sqrt{3}$ to $\text{Cr}_2\text{Ge}_2\text{Te}_6$ - 1×1 as shown by Fig. 1a. In heterostructure, the relative spacing and registry between $\text{Cr}_2\text{Ge}_2\text{Te}_6$ and In_2Se_3 are adjusted to find the energy minimum configuration. The reversal of the electric polarization of the isolated In_2Se_3 monolayer can be achieved via lateral displacement of the middle most Se layer, with an energy barrier as small as 0.04 eV per formula unit estimated by nudged elastic band calculation.²⁴ In heterostructure, due to the large vdW spacing, the presence of $\text{Cr}_2\text{Ge}_2\text{Te}_6$ does not noticeably affect the energy barrier of the electric polarization reversal process of In_2Se_3 . The total energy of the heterostructure is lowest (highest) where the interfacial Te atoms sit at the hollow (top) site of In_2Se_3 , with their relative energy difference amounts to 0.31 and 0.35 eV/u.c. for upward (Fig. 1b) and downward (Fig. 1c) polarizations, respectively. The equilibrium interlayer distance between $\text{Cr}_2\text{Ge}_2\text{Te}_6$ and In_2Se_3 at the hollow configuration is 3.20 and 3.14 \AA for up and down polarizations of In_2Se_3 , respectively. The total energy of the down polarization (Fig. 1c) is lower by 0.07 eV/u.c. than that of the up polarization (Fig. 1b), due to the stronger interfacial coupling between down-polarized In_2Se_3 and $\text{Cr}_2\text{Ge}_2\text{Te}_6$.

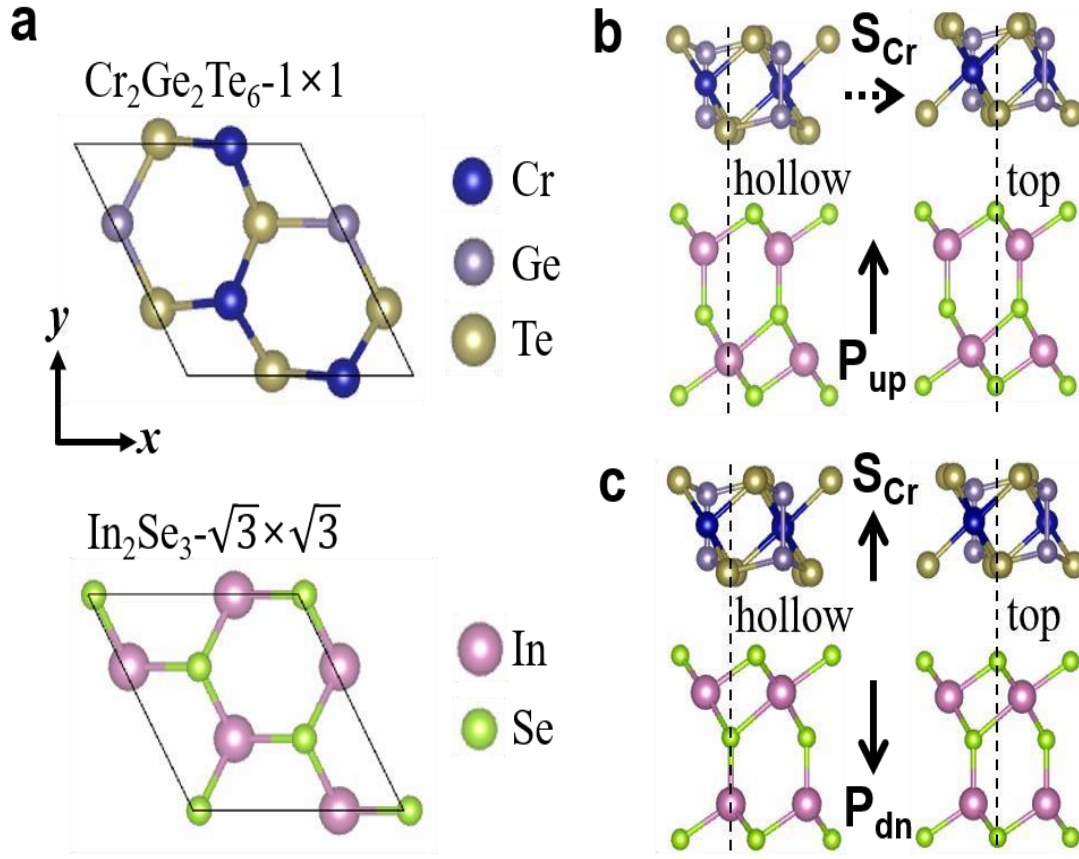


Figure 1. Van der Waals $\text{Cr}_2\text{Ge}_2\text{Te}_6/\text{In}_2\text{Se}_3$ heterostructure and magnetoelectric coupling. **a** Lateral unit cell size is chosen to be equal to that of ferromagnetic $\text{Cr}_2\text{Ge}_2\text{Te}_6$ experimental lattice constant and commensurate to ferroelectric $\text{In}_2\text{Se}_3-\sqrt{3} \times \sqrt{3}$ with -4 % strain. The interfacial two atomic layers (one atomic layer from each side of the interface) are shown in the top views of $\text{Cr}_2\text{Ge}_2\text{Te}_6-1 \times 1$ (top) and $\text{In}_2\text{Se}_3-\sqrt{3} \times \sqrt{3}$ (bottom). **b** and **c** Heterostructure side views with the In_2Se_3 ferroelectric dipole moment directed upward and downward (P_{up} and P_{dn}), respectively, and the induced easy-plane and easy-axis Cr spins (S_{Cr}). The solid (dashed) arrow of S_{Cr} indicates the allowed (prohibited) finite temperature long-range ferromagnetic ordering in 2D systems by the Mermin-Wagner theorem. For each case, the most stable (hollow) and unstable (top) stacking configurations are given.

In order to reproduce the experimental magnetic properties of bulk $\text{Cr}_2\text{Ge}_2\text{Te}_6$, we used small onsite Hubbard U value 0.5 eV and Hund's coupling J value 0.0 eV for Cr d -orbital in DFT calculations (see ref. 10 for the choice of $U = 0.5$ eV, $J = 0.0$ eV). This small onsite Coulombic interaction is consistent with the fact that $\text{Cr}_2\text{Ge}_2\text{Te}_6$ is a small band gap material with less localization than Cr-oxides. The ferromagnetic ground state is confirmed with the Cr spin magnetic moment $\sim 3.0 \mu_{\text{B}}$. With the spin orbit coupling (SOC) included, the magnetocrystalline anisotropy energy (MAE) is calculated and defined as $E_{[100]} - E_{[001]}$, where the former and latter correspond to the total energy with the Cr spins directed in-plane and out-of-plane, respectively. Due to the three-fold rotational symmetry of $\text{Cr}_2\text{Te}_2\text{Te}_6$, there is not much magnetic anisotropy within the basal plane. We checked the convergence of MAE carefully,

where a large value of K-mesh (12x12x1) was enough to ensure the error less than 10 $\mu\text{eV}/\text{Cr}$. For the isolated monolayer $\text{Cr}_2\text{Ge}_2\text{Te}_6$, our calculated MAE is -70 $\mu\text{eV}/\text{Cr}$, favoring the in-plane direction. In the heterostructures with up and down polarized In_2Se_3 , the calculated Cr MAE is -95 μeV and 75 μeV , respectively, whose energetically favorable spin orientations are indicated by \mathbf{S}_{Cr} in Fig. 1b,c. By modulating the polarization of the adjacent ferroelectric layer, the switching of the magnetization orientation is realized. This has significant application implications: For a 2D magnetic system with easy-plane anisotropy (X-Y model), the finite temperature ferromagnetic order is inhibited, whereas for easy-axis anisotropy (Ising model), the magnetic order can be sustained at finite temperatures. Therefore, in such a heterostructure, multiferroic effect offers a potential route to switch the ferromagnetism for logic devices.

The mechanism for electric-polarization dependent MAE is discussed in details. The calculated Cr orbital moment is small ($\langle L_x \rangle = 0.04 \mu_B$, $\langle L_z \rangle = 0.01 \mu_B$ for in-plane, out-of-plane spin directions), which is less likely the origin of MAE. The plausible mechanism is related to the detailed feature of spin-resolved orbital-decomposed band structure.²⁵ Starting from the collinear spin band structures, we analyzed the energy correction by the perturbation theory about $\lambda \mathbf{L} \cdot \mathbf{S}$ where λ is the radial part of Cr SOC. The orbital moment quenched by the crystal field results in the vanishing first order correction. Assuming the negligible change of the electron correlation energy between [100] and [001] spin directions, one can write the second order contribution to MAE as follows:²⁵

$$\text{MAE} = \lambda^2 \sum_{v,c,\sigma} (|\langle v, \sigma | L_z | c, \sigma \rangle|^2 - |\langle v, \sigma | L_x | c, \sigma \rangle|^2) / (\epsilon_{c,\sigma} - \epsilon_{v,\sigma}) + \lambda^2 \sum_{v,c,\sigma \neq \sigma'} (|\langle v, \sigma | L_x | c, \sigma' \rangle|^2 - |\langle v, \sigma | L_z | c, \sigma' \rangle|^2) / (\epsilon_{c,\sigma'} - \epsilon_{v,\sigma}), \quad (1)$$

Here the first and second summations correspond to the spin-conserving $|\Delta s_z| = 0$ and spin-flipping $|\Delta s_z| = 1$ transitions, and $|v, \sigma\rangle$ and $|c, \sigma\rangle$ are valence and conduction band states with spin σ , respectively, whose energy eigenvalues are $\epsilon_{c,\sigma}$ and $\epsilon_{v,\sigma}$. The angular momentum matrix elements of L_z and L_x correspond to transitions with $|\Delta m_z| = 0$ and $|\Delta m_z| = 1$, respectively, for Cr d -orbitals. Therefore, for spin-conserving transition, SOC elements between occupied and unoccupied states with the same (different) magnetic quantum number through the L_z (L_x) operator contributes to positive (negative) MAE. For spin-flipping transition, the contribution to MAE is reversed.²⁶

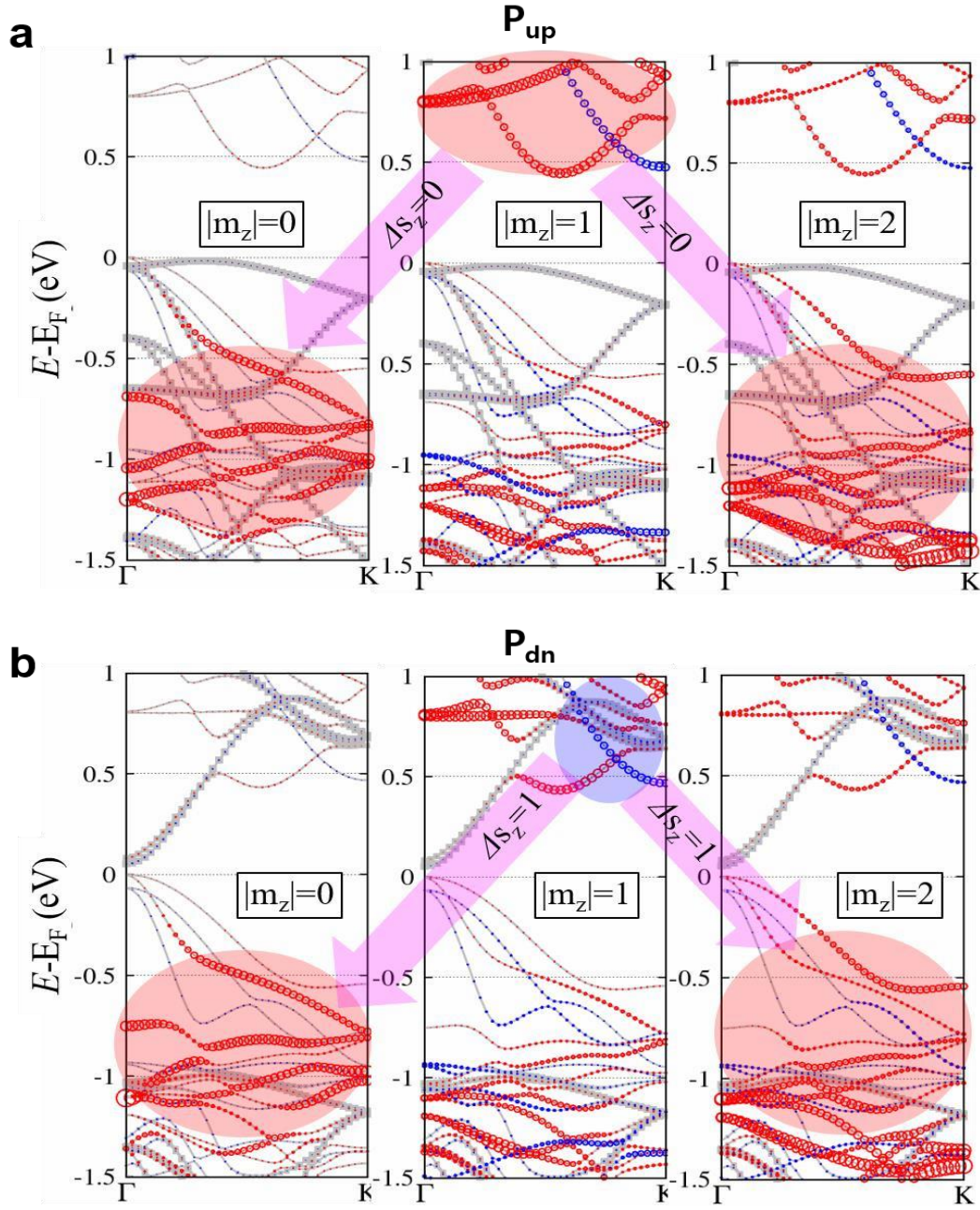


Figure 2. Spin-polarized and Cr d orbital-decomposed band structures of $\text{Cr}_2\text{Ge}_2\text{Te}_6/\text{In}_2\text{Se}_3$ heterostructures, a and b. The calculated band structures for the heterostructures with \mathbf{P}_{up} and \mathbf{P}_{dn} In_2Se_3 , respectively. The majority and minority spin states are indicated by the red and blue circles, respectively, whose size denotes the contribution of Cr d orbitals with certain azimuthal angular momentum $|m_z|$. In_2Se_3 states are shown by the gray dots, and the band exhibits the overall shift down by $\sim 1\text{eV}$ while changing In_2Se_3 from \mathbf{P}_{up} and \mathbf{P}_{dn} , which indicates a strong In_2Se_3 -polarization dependent interfacial coupling. The pink arrows indicate the SOC elements between empty and filled states, indicated by the red circle for the majority spin or blue for minority, causing the negative or positive value of MAE for a or b, respectively, thus the easy-plane or easy-axis Scr .

Fig. 2a,b shows the spin-resolved orbital-decomposed band structure of heterostructures for up- and down-polarized In_2Se_3 , respectively, where the contribution of Cr d -orbitals is indicated by the circles

for $|m_z| = 0$ (z^2), 1 (xz and yz), or 2 (x^2-y^2 and xy). As shown by the arrows in Fig. 2a for the heterostructure with up-polarized In_2Se_3 , our calculated negative MAE mainly originates from the spin-conserving transition from $|m_z| = 1$ to $|m_z| = 0$ or 2, i.e. $|\Delta s_z| = 0$ and $|\Delta m_z| = 1$ are related to the second term of the first sum in Eq. (1).

However, for the heterostructure with down-polarized In_2Se_3 , as shown in Fig. 2b, the conduction band minimum of Cr d $|m_z| = 1$ shows a large gap (~ 0.2 eV) near 0.5 eV above Fermi level, which is caused by hybridization with the In_2Se_3 conduction band minimum. Such hybridization results in a significant depletion of $|m_z| = 1$ majority spin DOS. Hence, the negative contribution to MAE found for the case of up-polarized In_2Se_3 is suppressed. Meanwhile the minority spin DOS remains almost unchanged for $|m_z| = 1$, leading to positive MAE via $|\Delta s_z| = 1$ and $|\Delta m_z| = 1$, as illustrated by the arrows in Fig. 2b. Considering the interfacial hybridization depends on the band alignment of In_2Se_3 and $\text{Cr}_2\text{Ge}_2\text{Te}_6$, we employed the Heyd-Scuseria-Ernzerhof exchange-correlation functional (HSE06) to recalculate the band properties of the heterostructures. As expected, the calculated band gaps widen compared with the GGA-PBE results, but the key features while In_2Se_3 reverses its electric orientation from up to down keep the same: the conduction band of In_2Se_3 moves down to hybridize with the conduction band of $\text{Cr}_2\text{Ge}_2\text{Te}_6$.

The sign change of $\text{Cr}_2\text{Ge}_2\text{Te}_6$'s MAE upon the electric polarization reversal of In_2Se_3 from up to down arises from the increased coupling, which causes the overall shift down of In_2Se_3 bands and its enhanced hybridization with $\text{Cr}_2\text{Ge}_2\text{Te}_6$. This suggests that the positive MAE for the down polarization would be enhanced by a reduced vdW spacing. To confirm this scenario, we did interlayer spacing dependent MAE calculations for hollow configuration as shown in Fig. 3. As the interlayer distance decreases, MAE increases gradually with a slight fluctuation. The fluctuation originates from the detailed variation of energy levels in the spin-polarized band structures. From the same calculation conducted for the top configuration, it exhibits a stronger fluctuation with the interlayer spacing, due to the larger degree of interfacial orbital overlap in top configuration. The same trend of the two curves in Fig. 3 confirms that the increased interlayer hybridization tends to switch the magnetocrystalline anisotropy from easy-plane to easy-axis.

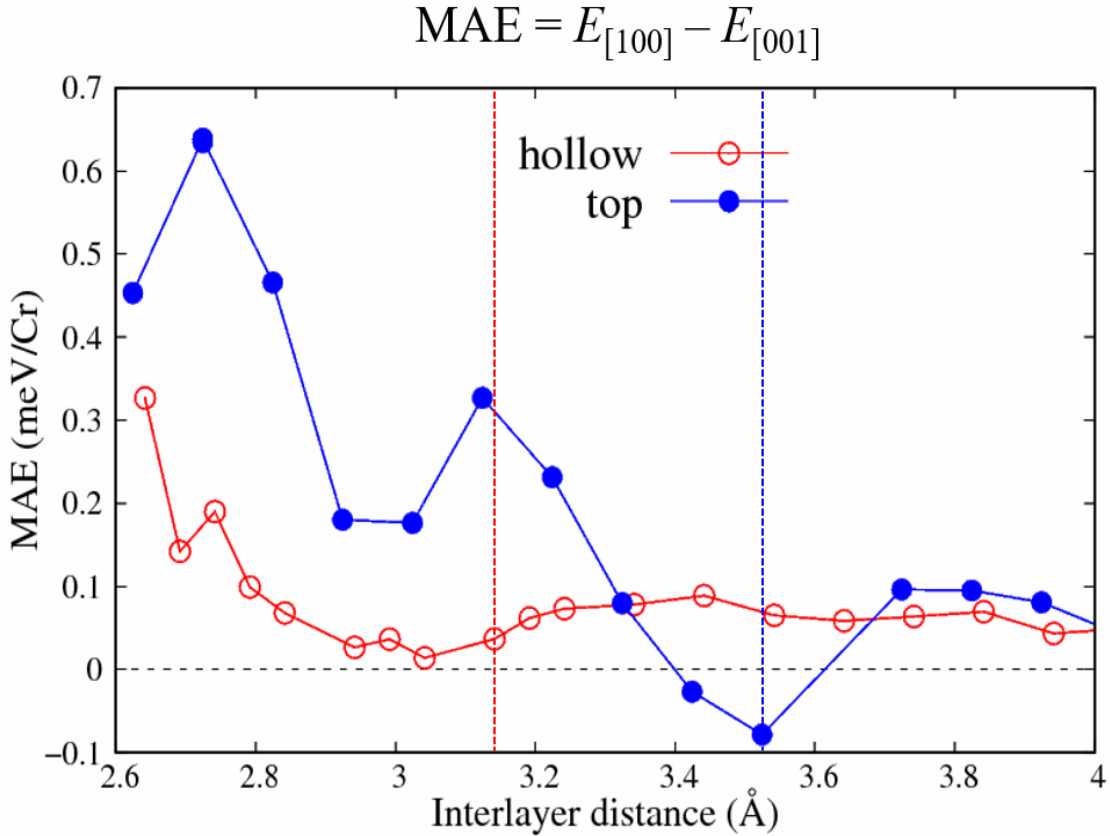


Figure 3. Calculated magnetocrystalline anisotropy of $\text{Cr}_2\text{Ge}_2\text{Te}_6$ in the heterostructure versus the vdW interlayer distance. Magnetocrystalline anisotropy energy (MAE) (in meV/Cr) of $\text{Cr}_2\text{Ge}_2\text{Te}_6$ as a function of the distance to In_2Se_3 in the \mathbf{P}_{an} state, showing a gradual increase towards the positive MAE (easy-axis S_{Cr}) upon decreasing the distance for both hollow and top stacking configurations. This set of calculations confirmed the scenario that the enhanced interfacial hybridization between $\text{Cr}_2\text{Ge}_2\text{Te}_6$ and In_2Se_3 tends to switch the magnetocrystalline anisotropy from easy-plane to easy-axis. The calculation error is reflected by the symbol size (~ 0.01 meV/Cr). The red and blue dashed lines correspond to the equilibrium interfacial distances for hollow and top stacking configurations, respectively.

Remarkably, the exchange splitting in Cr d -band magnetizes In_2Se_3 by the proximity effect. As shown in Fig. 2, the highest valence band has a significant exchange splitting, where the majority-spin band is closer to the Fermi level near Γ . Those states are mainly caused by the surface Te atoms in $\text{Cr}_2\text{Ge}_2\text{Te}_6$, which means the interfacial Te atoms have the electron spin antiparallel to that of Cr d electrons. Our calculated spin moment per Te atom is $-0.11 \mu_{\text{B}}$ for In_2Se_3 of either electric polarizations. Also, the surface In and Se atoms has non-zero spin moments parallel to Te spins induced by the proximity. The spin-resolved DOS of interfacial In and Se, shown in Fig. 4a, confirmed the magnetized In_2Se_3 . It is practically important to note the calculated magnetized In_2Se_3 here is a ground-state property. At finite temperatures, easy-plane magnetization of 2D In_2Se_3 is susceptible to thermal fluctuations and long-range order does not exist, but easy-axis magnetization of 2D In_2Se_3 could sustain the spin polarization at certain finite temperatures. Hence, a switching of 2D magnetic ferroelectric In_2Se_3 could be realized

in this heterostructure multiferroics, leading to a design of spin field-effect transistor.^{27,28}

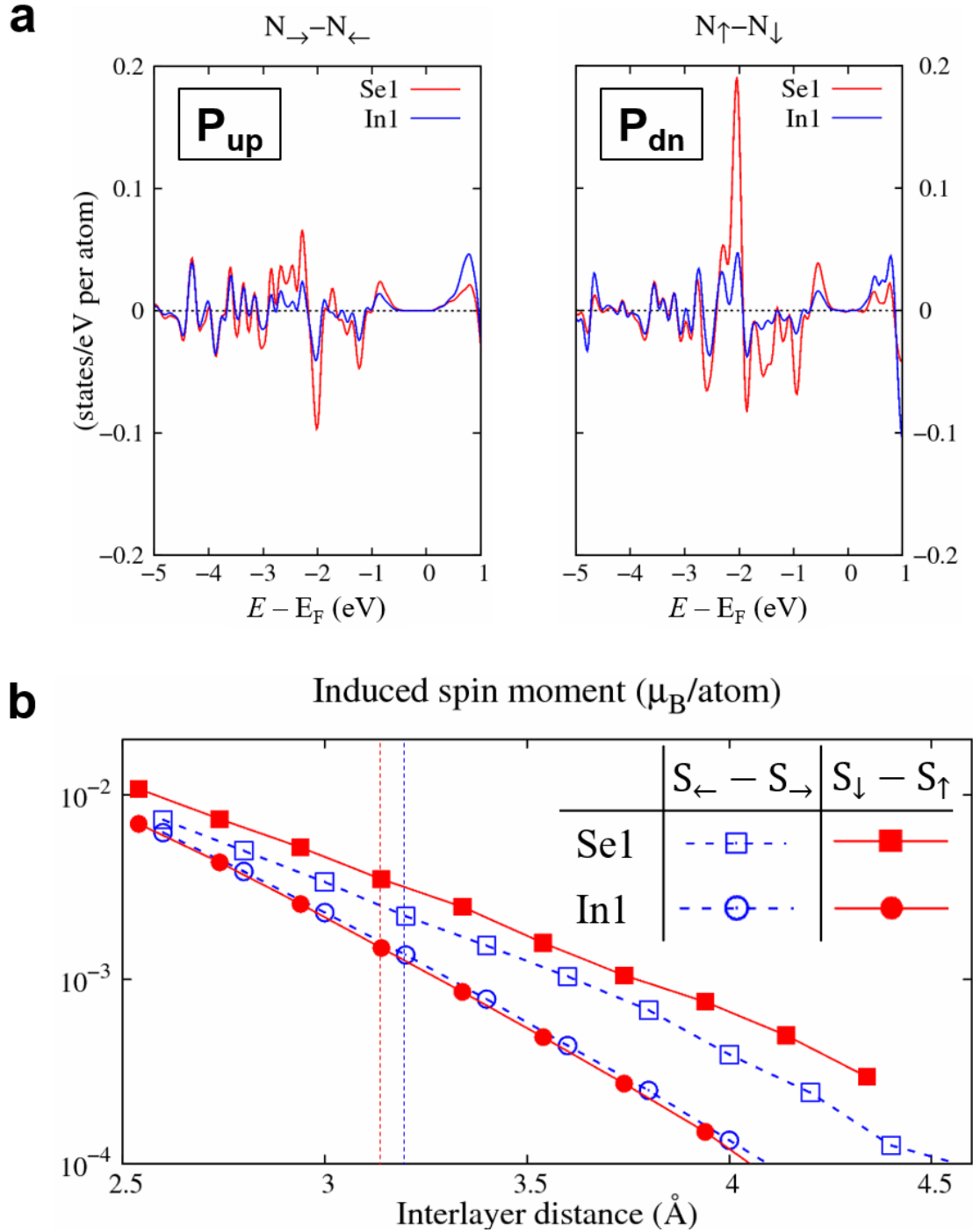


Figure 4. Magnetoelectric effect in In_2Se_3 , mediated by the magnetic proximity to $\text{Cr}_2\text{Ge}_2\text{Te}_6$. **a** Projected spin density of states for the surface (Se1) and subsurface (In1) atomic layers close to $\text{Cr}_2\text{Ge}_2\text{Te}_6$. Left and right panels correspond to the heterostructures with \mathbf{P}_{up} and \mathbf{P}_{dn} In_2Se_3 , respectively, with the in-plane and out-of-plane spin quantization axis. Given the prohibited long-range magnetic order for the easy-plane 2D magnetic system, the spin-polarized In_2Se_3 as shown by the left panel of **a** is only a ground state at zero Kelvin. But the easy-axis spin-polarized In_2Se_3 as shown by the right panel of **a** is practical at finite temperatures. Hence, the magnetization of the semiconducting In_2Se_3 can be switched by its own electric polarization, while in proximity to $\text{Cr}_2\text{Ge}_2\text{Te}_6$. **b** Interlayer distance dependence of the proximity induced Se1 and In1 spin

moments. The vertical dashed lines denote the equilibrium distances predicted by PBE with D2 vdW correction. Note that the induced spin moments are negative, which means the interlayer antiferromagnetic proximity effect in the studied In_2Se_3 - $\text{Cr}_2\text{Ge}_2\text{Te}_6$ heterostructures.

The induced spin moment of surface Se is attributed to the exchange coupling $J \sim t^2/U$ between Te p and Se p orbitals, with t the hopping constant and U the intra-orbital Coulomb repulsion. In the limit of zero t or infinite U , the system favors the triplet state similar to the atomic Hund coupling, which is the case for Te p and Se p . For a given value of U , the t varies exponentially with the distance. Consistently, our calculations show the exponentially increasing Se spin moment with decreased interfacial distance, as shown in Fig. 4b. The correlation effect should depend on the specific non-local correlation functional.

It is of experimental guidance to remark on the possible effects of real material environments. Calculation and analysis in this work are based on the heterostructure of a bilayer system floating in vacuum. In the experimental realization, the initial anisotropy of the magnetic layer $\text{Cr}_2\text{Ge}_2\text{Te}_6$ could be affected by a few factors, including contacting the materials of large dielectric constants^{22,29} or large SOC strengths,³⁰ unintentional doping³¹⁻³³ caused by chemicals in device fabrication process, and small amount of artificial strain induced in heterostructure preparation. These factors may affect the resultant magnetoelectric effect quantitatively : the increased U value enhances the out-of-plane anisotropy, while the increased J value enhances the in-plane anisotropy; for any tested set of U and J values, the out-of-plane anisotropy is always enhanced by ~ 0.15 meV/Cr when the In_2Se_3 dipole is inverted from up to down. Therefore, even if our adopted values of U and J ($U = 0.5$ eV, $J = 0.0$ eV) slightly deviate from the exact description of the real heterostructure samples because of the aforementioned complex experimental conditions, the reversal of the In_2Se_3 polarization from up to down always strengthens the 2D ferromagnetic order in $\text{Cr}_2\text{Ge}_2\text{Te}_6$. This leads to a general implication: in practice, one can always set a temperature so that 2D ferromagnetism could be found in $\text{P}_{\text{dn}}\text{-In}_2\text{Se}_3\text{-Cr}_2\text{Ge}_2\text{Te}_6$ but disappear from $\text{P}_{\text{up}}\text{-In}_2\text{Se}_3\text{-Cr}_2\text{Ge}_2\text{Te}_6$, leading to the practical switching experiments at finite temperatures. Therefore, the magnetoelectric effect presented here, based on the modification of MAE by the intricate interface hybridization which further relates to the electric polarization of the 2D ferroelectrics, is an intrinsic interfacial phenomenon.

I.4 Conclusion

We employed first-principles DFT calculations on a vdW heterostructure consisting of ferromagnetic $\text{Cr}_2\text{Ge}_2\text{Te}_6$ and ferroelectric In_2Se_3 monolayers. By reversing the electric polarization of In_2Se_3 , the calculated magnetocrystalline anisotropy of $\text{Cr}_2\text{Ge}_2\text{Te}_6$ changes between easy-axis and easy-plane (i.e., switching on/off of the ferromagnetic order), which promises a novel design of magnetic memory. Furthermore, In_2Se_3 becomes magnetic ferroelectrics, with switchable spin polarizations according to its own electric polarization. The 2D multiferroic heterostructures would tremendously enlarge the landscape of multiferroics by artificially assembling 2D layers and provide new material platforms for a plethora of emergent interfacial phenomena.

I.5 References

1. Wang, J. et al. Epitaxial BiFeO_3 multiferroic thin film heterostructures. *Science* **299**, 1719 (2003).
2. Kimura, T. et al. Magnetic control of ferroelectric polarization. *Nature* **426**, 55 (2003).
3. Ramesh, R. & Spaldin, N. A. Multiferroics: progress and prospects in thin films. *Nat. Mater.* **6**, 21 (2007).
4. Fiebig, M. et al. Revival of the magnetoelectric effect. *J. Phys. D* **38**, R123 (2005).
5. Fiebig, M. et al. The evolution of multiferroics. *Nat. Rev. Mater.* **1**, 16046 (2016).
6. Cheong, S.-W. & Mostovoy, M. Multiferroics: a magnetic twist for ferroelectricity. *Nat. Mater.* **6**, 13 (2007).
7. Hill, N. A. Why are there so few magnetic ferroelectrics? *J. Phys. Chem. B* **104**, 6694 (2000).
8. Zheng, H. et al. Multiferroic BaTiO_3 - CoFe_2O_4 Nanostructures. *Science* **303**, 661 (2004).
9. Geim, A. K. & Grigorieva, I. V. Van der Waals heterostructures. *Nature* **499**, 419 (2013).
10. Gong, C. et al. Discovery of intrinsic ferromagnetism in two-dimensional van der Waals crystals. *Nature* **546**, 265-269 (2017).
11. Huang, B. et al. Layer-dependent ferromagnetism in a van der Waals crystal down to the monolayer limit. *Nature* **546**, 270-273 (2017).
12. Gong, C. & Zhang, X. Two-dimensional magnetic crystals and emergent heterostructure devices. *Science* **363**, eaav4450 (2019).

13. Liu, F. et al. Room-temperature ferroelectricity in CuInP₂S₆ ultrathin flakes. *Nat. Commun.* **7**, 12357 (2016).
14. Seixas, L., Rodin, A. S., Carvalho, A. & Castro Neto, A. H. Multiferroic two-dimensional materials. *Phys. Rev. Lett.* **116**, 206803 (2016).
15. Wang, H. & Qian, X. Two-dimensional multiferroics in monolayer group IV monochalcogenides. *2D Mater.* **4**, 015042 (2017).
16. Luo, W., Xu, K. & Xiang, H., Two-dimensional hyperferroelectric metals: a different route to ferromagnetic-ferroelectric multiferroics. *Phys. Rev. B* **96**, 235415 (2017).
17. Qi, J., Wang, H., Chen, X. & Qian X., Two-dimensional multiferroic semiconductors with coexisting ferroelectricity and ferromagnetism. *Appl. Phys. Lett.* **113**, 043102 (2018).
18. Ding, W. et al. Prediction of intrinsic two-dimensional ferroelectrics in In₂Se₃ and other III₂-VI₃ van der Waals materials. *Nat. Commun.* **8**, 14956 (2017).
19. Zhou, Y. et al. Out-of-plane piezoelectricity and ferroelectricity in α -layered In₂Se₃ nanoflakes. *Nano Lett.* **17**, 5508-5513 (2017).
20. Cui, C. et al. Intercorrelated in-plane and out-of-plane ferroelectricity in ultrathin two-dimensional layered semiconductor In₂Se₃. *Nano Lett.* **18**, 1253-1258 (2018).
21. Xiao, J. et al. Intrinsic two-dimensional ferroelectricity with dipole locking. *Phys. Rev. Lett.* **120**, 227601 (2018).
22. Mermin, N. D. & Wagner, H. Absence of Ferromagnetism or Antiferromagnetism in One- or Two-Dimensional Isotropic Heisenberg Models. *Phys. Rev. Lett.* **17**, 1133 (1966).
23. Bruno, P. Magnetization and Curie temperature of ferromagnetic ultrathin films: the influence of magnetic anisotropy and dipolar interactions. *Mater. Res. Symp. Proc.* **231**, 299-310 (1991).
24. Henkelman G. A climbing image nudged elastic band method for finding saddle points and minimum energy paths. *J. Chem. Phys.* **113**, 9901-9904 (2000).
25. Wang, D. et al. First-principles theory of surface magnetocrystalline anisotropy and the diatomic-pair model. *Phys. Rev. B* **47**, 14932 (1993).
26. Sui, X. et al. Voltage-controllable colossal magnetocrystalline anisotropy in single-layer transition metal dichalcogenides. *Phys. Rev. B* **96**, 041410 (2017).
27. Datta, S. & Das, B. Electronic analog of the electro-optic modulator. *Appl. Phys. Lett.* **56**, 665-667 (1990).

28. Gong, S.-J. et al. Electrically induced 2D half-metallic antiferromagnets and spin field effect transistors. *Proc. Natl. Acad. Sci.* **115**, 8511-8516 (2018).
29. Jiang, S., Shan, J. & Mak, K. F. Electric-field switching of two-dimensional van der Waals magnets. *Nat. Mater.* **17**, 406-410 (2018).
30. Avsar, A. et al. Spin-orbit proximity effect in graphene. *Nat. Commun.* **5**, 4875 (2014).
31. Huang, B. et al. Electrical control of 2D magnetism in bilayer CrI₃. *Nat. Nanotechnol.* **13**, 544-548 (2018).
32. Jiang, S., Li, L., Wang, Z., Mak, K. F. & Shan, J. Controlling magnetism in 2D CrI₃ by electrostatic doping. *Nat. Nanotechnol.* **13**, 549-553 (2018).
33. Wang, Z. et al. Electric-field control of magnetism in a few-layered van der Waals ferromagnetic semiconductor. *Nat. Nanotechnol.* **13**, 554-559 (2018).
34. Kresse, G. & Furthmüller, J. Efficiency of ab-initio total energy calculations for metals and semiconductors using a plane-wave basis set. *Comput. Mater. Sci.* **6**, 15-50 (1996).
35. Perdew, J. P., Burke, K. & Ernzerhof, M. Generalized gradient approximation made simple. *Phys. Rev. Lett.* **77**, 3865 (1996).
36. Grimme, S. Semiempirical GGA-type density functional constructed with a long-range dispersion correction. *J. Comp. Chem.* **27**, 1787 (2006).

I. Edge Functionalized Graphene Nanoribbons with tunable band alignments for Carrier Transport Interlayer in Organic-Inorganic Perovskite Solar Cells

II.1 Introduction

Since the first report of photovoltaic power conversion efficiency (PCE) of 3.8 % based on perovskite light absorber materials, $\text{CH}_3\text{NH}_3\text{PbX}_3$ (X=Br, I),⁸ a lot of efforts have been devoted to improving the efficiency by solvent engineering for less defects,⁶ tunable band gap by halides mixing,¹¹ thin film or tandem architectures,²² and so on. Recently the certified efficiency has reached up to 24.2%.³ Owing to its solution processing, it is beneficial for massive production with low cost. However the issues still exists for commercialization, for example, structural and environmental stabilities, replacing toxic Pb, large-area uniform deposition, etc.. Nevertheless, the lead halide perovskite provides great opportunity to explore distinguishing features that are attributed to excellent carrier transport behavior, such as defect tolerance⁵ and dynamical role of organic cations,¹⁵ which are essentially absent in conventional inorganic material based system.

In spite of micrometre scale carrier diffusion length within MAPbI_3 ,²⁰ the overall efficiency is affected critically by the details of interface to carrier extraction layers of electron transport material (ETM), hole transport material (HTM), where a typical device structure is $\text{FTO}/\text{TiO}_2/\text{MAPbI}_3/\text{Spiro-OMeTAD}/\text{Au}$. Besides either porous or compact TiO_2 as ETM, an elemental doping or other metal oxides such as SnO_2 , ZnO , Nb_2O_5 have been studied to improve the stability against J-V hysteresis.^{21,24} Especially La-doped BaSnO_3 replacing TiO_2 showed one thousand hours stable performance with PCE as high as 22 % .¹⁹ The conduction band edge of bulk ETM materials has been considered for a proper band alignment. However, the role of structural defects and trap states at the interface of ETM and MAPbI_3 is largely unknown. As for HTM, the thermal stability has been improved by replacing the commonly used organic layer (spiro-OMETAD) with CuCSN .¹ As compared to organic counterparts, a stronger electronic coupling achievable between inorganic carrier extraction layers and usually PbI_2 terminated surface will be suitable for improving charger transfer as well as stability. However, many studies have introduced organic interlayers composed of fullerene or its derivative so as to have a better performance,¹⁸ which suggests that the presence of an organic interlayers with a proper band alignment might be helpful. Furthermore, during device fabrication, inorganic carrier extraction layers would

require high temperature processing which can induce a lot of structural disorder in organic-inorganic perovskite. In this paper, we propose to use the graphene nanoribbons (GNRs) as the interlayers. GNRs can be synthesized by unzipping the carbon nanotubes [Kosynikin2009]. Its solution process can be easily employed in MAPbI₃ growth and fabrication. Also as improved performance by introducing fullerene derivatives as interlayers, organic based GNRs can be helpful to improve the device performance.

Here we calculate the electronic structure of edge functionalized GNRs as carrier extraction interlayers. Edge functionalization by hydrogen and fluorine is considered to tailor the band alignment with respect to MAPbI₃ as well as to tune the band gap by varying the width.

II.2 Computational Method

All calculations have been performed by using the DFT method as implemented in VASP code (Vienna ab initio simulation package).¹⁰ The plane wave energy cutoff of default value was used with PBE parameterization of GGA exchange-correlation functional.¹⁶ In case of MAPbI₃, the spin-orbit coupling (SOC) is included for proper description of electronic energy levels. Also the hybrid functional of PBE0 type is used to calculate the energy gap and the band edge levels accurately, which will be used for reliable prediction of the band alignment for the heterostructures.^{4,14} For MAPbI₃ crystal, the room temperature phase of tetragonal (I4/mcm)²³ is considered, where the lattice parameters are $a = 8.80 \text{ \AA}$, $c = 12.69 \text{ \AA}$, as shown in Fig. 6a. For GNRs, the armchair edge type is considered with its width seven carbon atoms long along a zigzag chain. It is noted that the width of GNR and the type of edge functional groups can be varied for a proper band alignment with MAPbI₃. A GNR with both edges passivated by hydrogen (HGNR) and fluorine (FGNR) are shown in Fig. 6b and 6c, respectively. In case of HGNR the ribbon shape is perfectly flat, but for FGNR it is rippled to minimize the Coulomb repulsion between in-plane p orbital electrons of F. The atomic positions are optimized until the force is less than 0.01 eV/Å with the van der Waals correction by Tkatchenko and Scheffler (TS) method.² The used k-mesh is 2x2x1 for the tetragonal MAPbI₃, 1x1x1 for HGNR and 1x1x1 for FGNR.

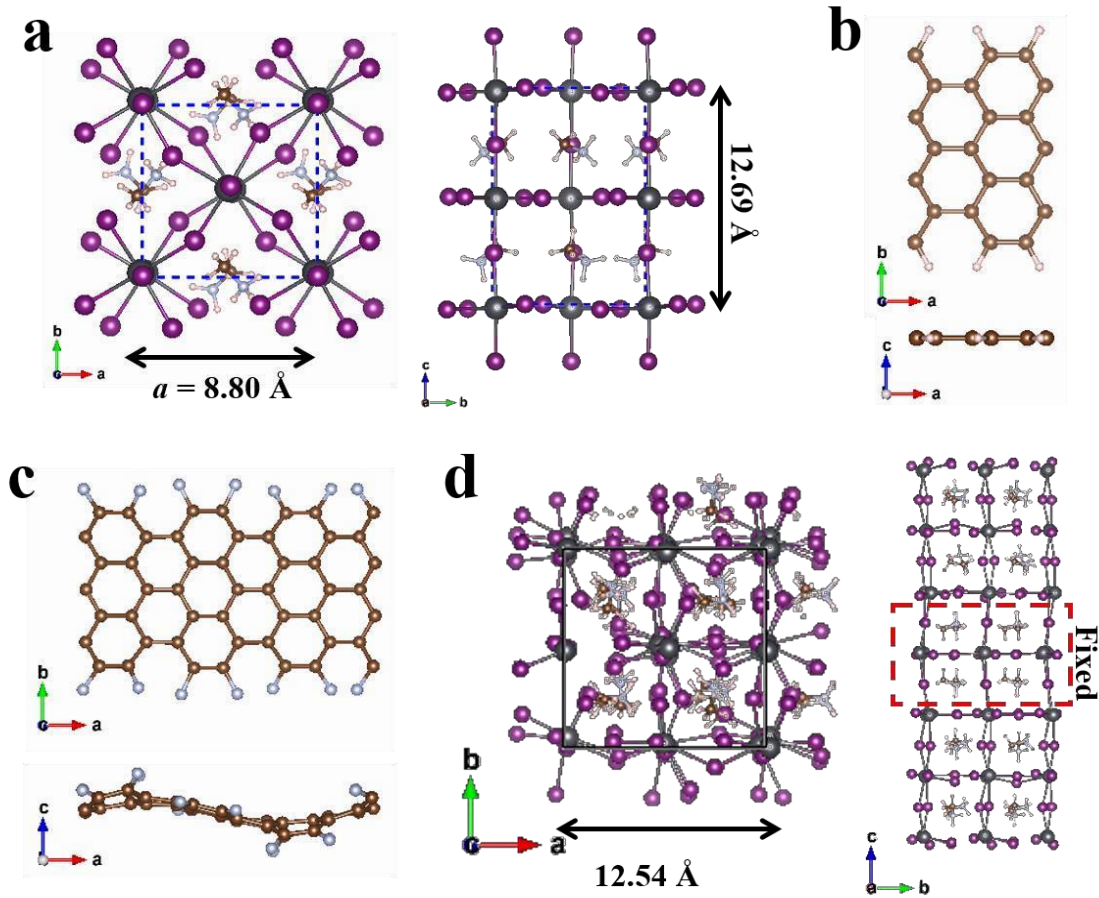


Figure 5. Structures of (a) MAPbI₃ (I₄/mcm) (b) H-GNR (c) F-GNR and (d) Clean MAPbI₃(001)

For the hetero-interface of MAPbI₃ and an edge functionalized GNR, we consider a symmetric six-layer slab model of PbI₂ terminated MAPbI₃(001) surface with a vacuum size of 10 Å, as shown in Fig. 5d. The in-plane lattice size is extended to $\sqrt{2} \times \sqrt{2}$ of the tetragonal unit with the adjusted lattice parameter 12.54 Å, which corresponds to 1.8 % reduction of GNR along the axis direction and 0.8 % in-plane expansion of MAPbI₃. Also the orientational configuration of the MA dipoles is chosen to be that of the body-centered tetragonal and mirror-reflected with respect to the central PbI₂ layer. The dipole correction is included to avoid an unphysical interaction between periodic images. Atomic positions of the central PbI₂ layer and the adjacent MAI layers are fixed as the bulk positions, and all the other atoms are optimized until the force is less than 0.01 eV/Å with the 1x1x1 k-mesh, where the vdW correction is included by TS method.² Once the structural optimization is done, the charge self-consistent calculation is performed by including the SOC, and the resulting charge density is used for calculations of the Density Of States (DOS) with 2x2x1 k-mesh or the band structure within PBE+SOC level.

II.3 Results and Discussion

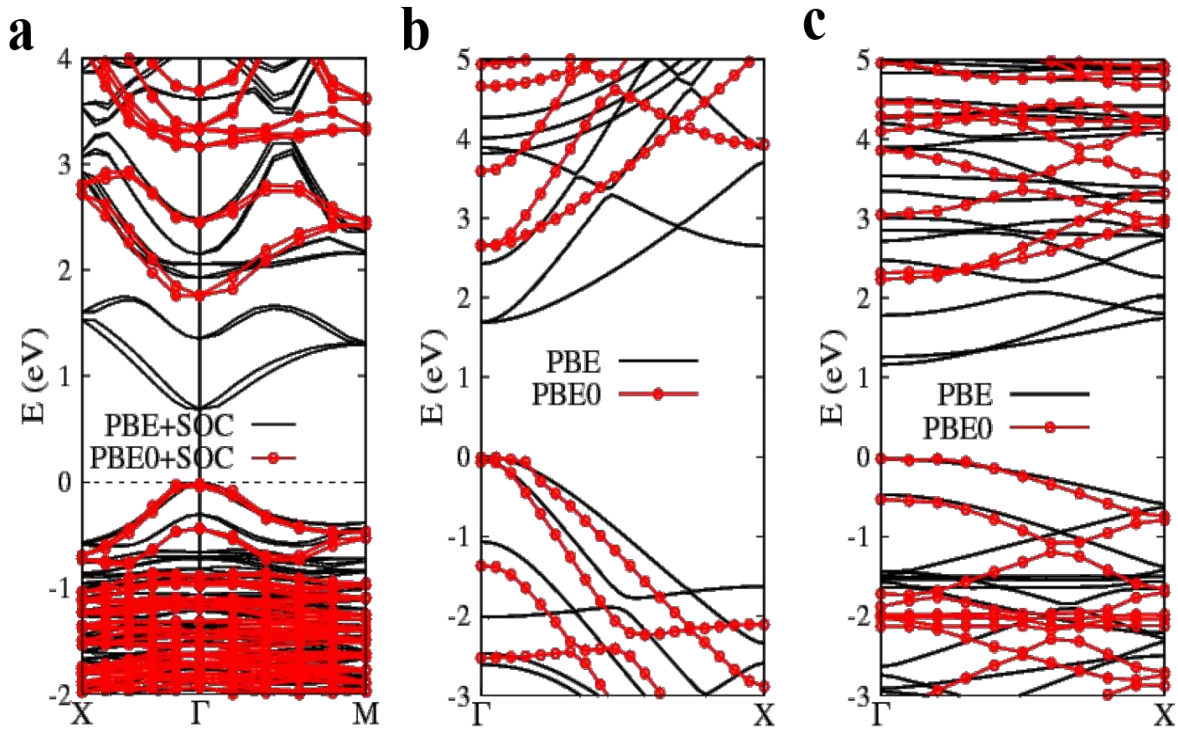


Figure 6. Band structures of (a) MAPbI₃ (b) H-GNR (c) F-GNR

Fig. 6 shows the band structures of the tetragonal MAPbI₃, H-GNR and F-GNR by PBE and PBE0 functionals. For MAPbI₃, the significantly underestimated band gap (0.69 eV) by PBE+SOC is increased to 1.78 eV by PBE0+SOC, which is consistent with the experimental value (~1.6 eV).¹² Also for H-GNR and F-GNR, the calculated energy gap is significantly increased when we use PBE0 as compared to using PBE, 2.66 (1.68) for H-GNR and 2.24 (1.14) for F-GNR by PBE0 (PBE). For H-GNR, the valence band maximum (VBM) and the conduction band minimum (CBM) states at Γ is doubly degenerate, while it is split for F-GNR. This is due to an additional presence of out-of-plane p_z orbital of F which forms a pi bond with edge carbon atom p_z orbital.

The valence and conduction band states of GNRs, which are composed of carbon pi orbitals, exhibits the quantum confinement effect by the size of ribbon wide. By varying the width, one can change the energy gap of GNRs. Also with varying the edge functional groups, the energy levels can be tuned.

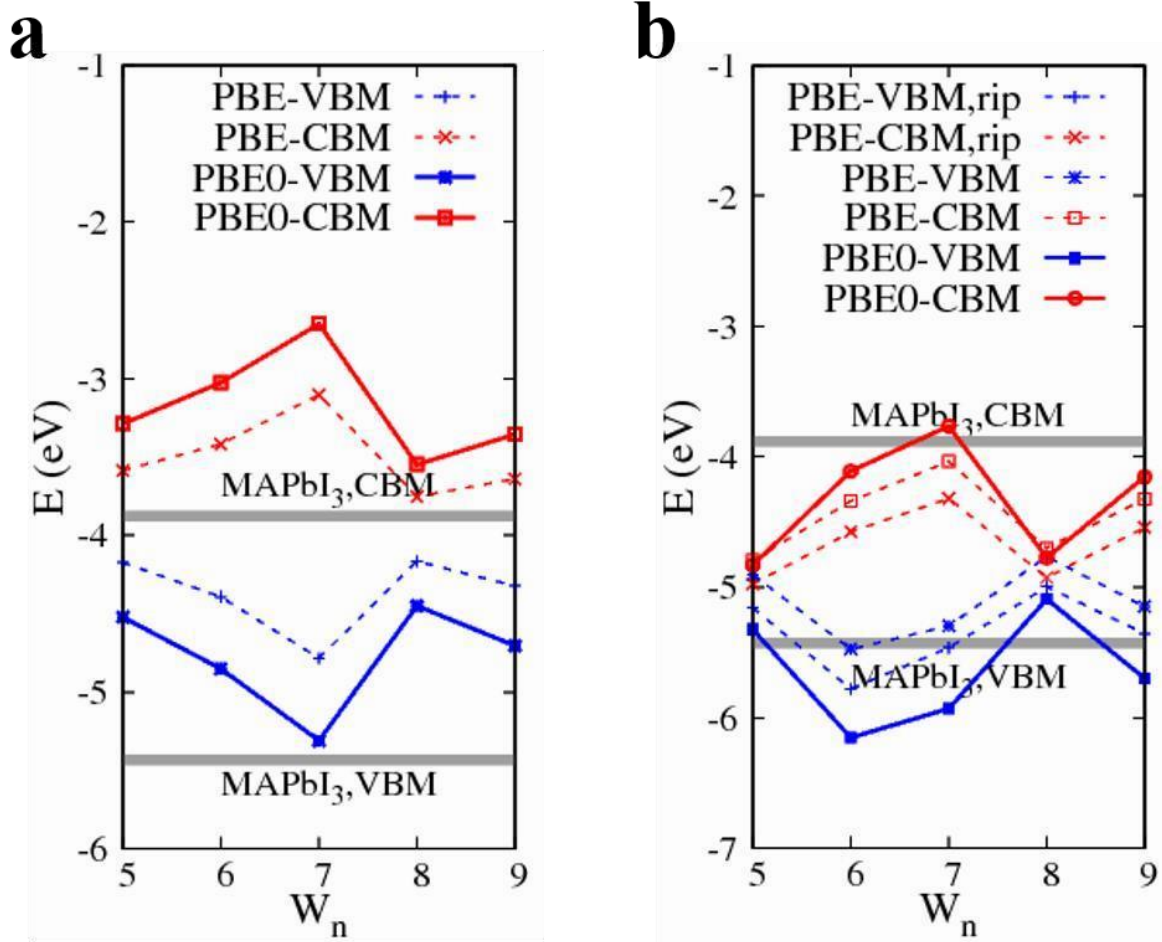


Figure 7. Band alignments of (a) H-GNR and (b) F-GNR

Fig. 7 shows our calculated energy levels of VBM and CBM for H-GNR and F-GNR with varying the width W_n from five to nine which denotes the number of carbon atoms along the transverse zigzag chain. When $W_n = 3p+2$, where p is integers, the size of gap is smaller than other cases $W_n = 3p$ and $3p+1$. Also the same type of W_n , the gap decreases gradually due to the quantum confinement. For H-GNR, shown in Fig. 7, the overall level of CBM (VBM) is higher than the experimental CBM (VBM) position of MAPbI_3 , -3.88 (-5.43) eV indicated by the horizontal gray line. This indicates that H-GNR is good for electron-blocking and hole-extraction interlayer. On the other hand, in case of F-GNR, the CBM and VBM shifts down significantly. The CBM of F-GNR lies lower than MAPbI_3 CBM, where the rippled structure shows a further lowering by about 0.2 eV from PBE result. Also the VBM is lower than the VBM of MAPbI_3 . This indicates that F-GNR will be good for electron-extraction and hole-blocking interlayer. It is noted that the VBM and CBM of MAPbI_3 in Fig. 7 are the experimental results. But it has been shown that the energy level is significantly influenced by the surface termination type, where we obtain -5.84 (-6.52) eV for CBM (VBM) for the PbI_2 terminated $\text{MAPbI}_3(001)$ similar to the reported value.¹⁷ Nevertheless, our results on the hetero interface show a desirable band

alignment, as will be shown.

In order to check the interface electronic structures, we performed PBE+SOC calculations for the heterostructures. By using $2\sqrt{2}\times\sqrt{2}$ lateral size of slab with the thickness of six periodic units, H-GNR or F-GNR is adsorbed on the MAPbI₃(001), whose optimized structures are shown in Fig. 8a or 9b, respectively. The adsorption energy is calculated to be -1711.587eV and -1716.694 for H-GNR and F-GNR, respectively. Significantly rippled structure in F-GNR allows a closer distance between F and PbI₂ layer as compared to H-GNR.

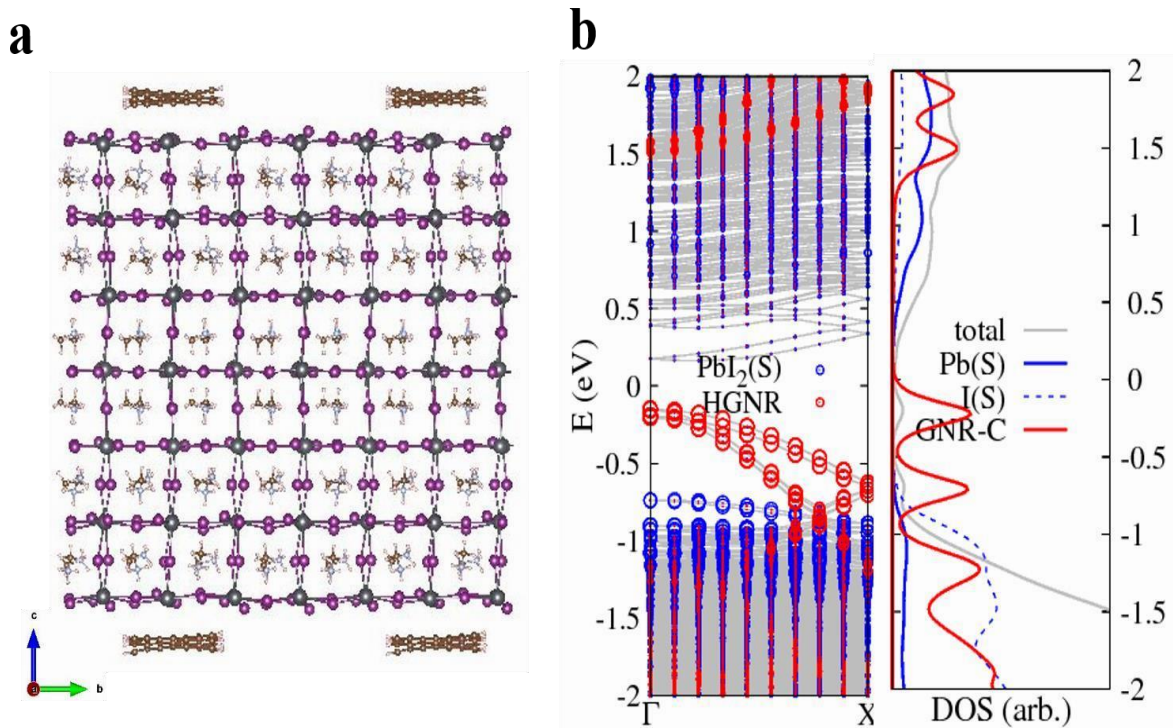


Figure 8. (a) Optimized structure (b) Band structure and Density Of States of H-GNR/MAPbI₃

Calculated band structure and density of states for H-GNR on MAPbI₃(001) are shown in Fig. 8b. The density of states at the PbI₂ surface layer, shown by the blue circles in the band structure, is compared with the H-GNR VBM or CBM. VBM of H-GNR is fairly above the occupied PbI₂ surface band, whereas the CBM of H-GNR is above the empty PbI₂ surface band. As also shown in density of states, the hole state by surface I (dashed blue line in the DOS plot) can be relaxed to H-GNR hole state, but the electron state by surface Pb (solid blue line) is blocked. Thus H-GNR can be a good interlayer for extracting holes and blocking electrons.

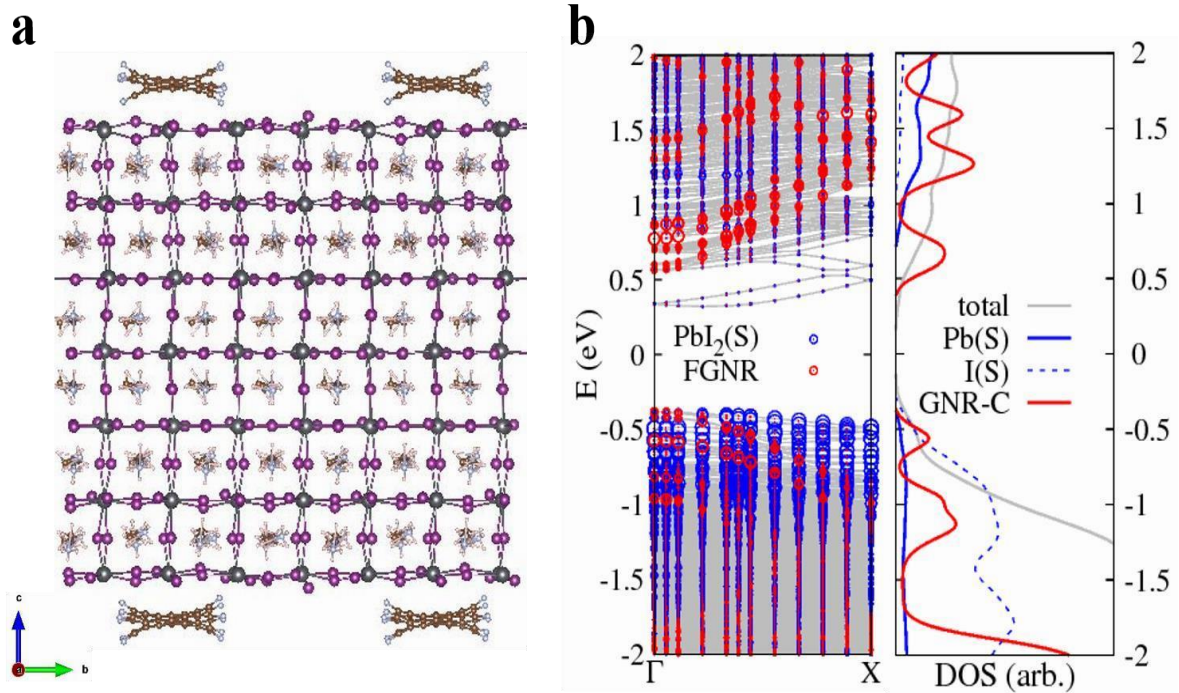


Figure 9. (a) Optimized structure (b) Band structure and Density Of States of F-GNR/MAPbI₃

The result of F-GNR heterostructure is shown in Fig. 9b. It is noted that the PbI₂ surface states appear above the conduction band edge for the empty states. This may indicate that the electron carriers need a sufficient energy to arrive at the interface. Our interface electronic structure shows that F-GNR CBM actually lies below the PbI₂ surface states. Although F-GNR VBM is nearly at the same energy level as that of the occupied PbI₂ surface states, it will be further lowered if PBE0 correction is included or a narrower width of F-GNR (e.g. W_n=6) as shown in Fig. 6b. Thus F-GNR can be a good interlayer for extracting electrons and blocking holes.

II.4 Conclusion

DFT based calculations were performed to study the interface electronic structures between edge functionalized armchair edge GNRs and MAPbI₃(001). It is suggested that the GNR edge group type and width can be tailored in order to have a proper band alignment with MAPbI₃ or other types of perovskite light absorbing materials.

II.5 References

1. Arora, N.; Dar, M. I.; Hinderhofer, A.; Pellet, N.; Schreiber, F.; Zakeeruddin, S. M.; Grätzel, M. Perovskite solar cells with CuSCN hole extraction layers yield stabilized efficiencies grather than 20%. *Science*. **2017**, *358*, 768-771.
2. Bučko, T.; Lebègue, s.; Hafner, J.; Ángyán, J. G. Tkatchenko-Scheffler van der Waals correction method with and without self-consistent screening applied to solids. *Phys. Rev. B*. **2013**, *87*, 064110.
3. National Renewable Energy Laboratory. Best research-cell efficiency chart. <https://www.nrel.gov/pv/assets/images/efficiency-chart.png> (2018).
4. Hinuma, Y.; Grüneis, A.; Kresse, G.; Oba, F. Band alignment of semiconductors from density-functional theory and many-body perturbation theory. *Phys. Rev. B*. **2014**, *90*, 155405.
5. Huang, H.; Bodnarchuk, M. I.; Kershaw, S. V.; Kovalenko, M. V.; Rogach, A. L. Lead Halide Perovskites Nanocrystals in the Research Spotlight: Stability and Defect Tolerance. *ACS Energy Lett*. **2017**, *2*, 2071-2083.
6. Jeon, N. J.; Noh, J. H.; Kim, Y. C.; Yang, W. S.; Ryu, S.; Seok, S. I. Solvent engineering for high-performance inorganic-organic hybrid perovskite solar cells. *Nature Materials*. **2014**, *13*, 897– 903.
7. Jiang, Q.; Zhang, L.; Wang, H.; Yang, X.; Meng, J.; Liu, H.; Yin, Z.; Wu, J.; Zhang, X.; You, J. Enhanced electron extraction using SnO₂ for high-efficiency planar-structure HC(NH₂)₂PbI₃- based perovskite solar cells. *Nature Energy*. **2016**, *2*, 16177.
8. Kojima, A.; Teshima, K.; Shirai, Y.; Miyasaka, T. Organometal Halide Perovskites as Visible-Light Sensitizers for Photovoltaic Cells. *J. Am. Chem. Soc*. **2009**, *131*, 6050-6051.
11. Kosynkin, D. V.; Higginbotham, A. L.; Sinitskii, A.; Lomeda, J. R.; Dimiev, A.; Price, K.; Tour, J. M. Longitudinal unzipping of carbon nanotubes to form graphene nanorribons. *Nature*. **2009**, *458*, 872– 876.
10. Kresse, G.; Furthmijller, F. Efficiency of ab-initio total energy calculations for metals and semiconductor using a plane-wave basis set. *Computational Materials Science* **6**. **1996**, *6*, 15-50.
11. Kulkarni, S. A.; Baikie, T.; Boix, P. P.; Yantara, N.; Mathews, N.; Mhaisalkar, S. Band-gap turning of lead halide perovskites using a sequential deposition process. *J. Mater. Chem. A*. **2014**, *2*, 9221-9225.
12. Lindblad, R.; Bi, D.; Park, B. W.; Oscarsson, J.; Gorgoi, M.; Siegbahn, H.; Odelius, M.; Johansson, E. J.; Rensmo, H. Electronic Structure of TiO₂/CH₃NH₃PbI₃ Perovskite Solar Cell Interfaces. *J. Phys. Chem. Lett*. **2014**, *5*, 648-653.
13. Meng, L.; You, J.; Yang, Y. Addressing the stability issue of perovskite solar cells for

commercial applications. *Nature Communications*. **2018**, *9*, 5265.

14. Menéndez-Proupin, E.; Palacios, P.; Wahnón, P.; Conesa, J. C. Self - consistent relativistic band structure of the $\text{CH}_3\text{NH}_3\text{PbI}_3$ perovskite. *PHYSICAL REVIEW B*. **2014**, *90*, 045207.

15. Myung, C. W.; Yun, J.; Kim, K. S.; Lee, G. S. A New Perspective on the Role of A- Site Cations in Perovskite Solar Cells. *Adv. Energy Mater.* **2018**, *8*, 1702898.

16. Perdew, J. P.; Burke, K.; Ernzerhof, M. Generalized Gradient Approximation Made Simple. *Phys. Rev. Lett.* **1996**, *77*, 3865.

17. Quarti, C.; Angelis, F. D.; Beljonne, D. Influence of Surface Termination on the Energy Level Alignment at the $\text{CH}_3\text{NH}_3\text{PbI}_3$ Perovskite/C60 Interface. *Chem. Mater.* **2017**, *29*, 958- 968.

18. Shao, Y.; Xiao, Z.; Bi, C.; Yuan, Y.; Huang, J. Origin and elimination of photocurrent hysteresis by fullerene passivation in $\text{CH}_3\text{NH}_3\text{PbI}_3$ planar heterojunction solar cells. *Nature Communications*. **2014**, *5*, 5784.

19. Shin, S.S.; Yeom, E. J.; Yang, W. S.; Hui, S.; Kim, M. G.; Im, J.; Seo, J.; Noh, J. H.; Seok, S. I. Colloidally prepared La-doped BaSnO_3 electrodes for efficient ,photostable perovskite solar cells. *Science*. **2017**, *356*, 167-171.

20. Stranks, S. D.; Eperon, G. E.; Grancini, G.; Menelaou, C.; Alcocer, M. J. P.; Leijtens, T.; Herz, L. M.; Petrozza, A.; Snaith, H. J. Electron-Hole Diffusion Lengths Exceeding 1 Micrometer in an Organometal Trihalide Perovskite Absorber. *Science*. **2013**, *342*, 341-344.

21. Tress, W.; Moehl, M. T.; Zakeeruddin, S. M.; Nazeeruddin, M. K.; Grätzel, M.; Understanding the rate-dependent J-V hysteresis, slow time component, and aging in $\text{CH}_3\text{NH}_3\text{PbI}_3$ perovskite solar cells: the role of a compensated electric field. *Energy Environ. Sci.* **2015**, *8*, 995–1004.

22. Werner, J.; Weng, C. H.; Walter, A.; Fesquet, L.; Seif, J. P.; Wolf, S. D.; Niesen, B.; Ballif, C. Efficient Monolithic Perovskite/Silicon Tandem Solar Cell with Cell Area > 1 cm^2 . *J. Phys. Chem. Lett.* **2016**, *7*, 161-166.

23. Whitfield, P. S.; Guise, H. W. E.; Cheng, Y. Q.; Millar, I.; Crawford, M. K. Structures, Phase Transitions and Tricritical Behavior of the Hybrid Perovskite Methyl Ammonium Lead Iodide. *Scientific Reports*. **2016**, *6*, 35685.

24. Zhao, Y.; Liang, C.; Zhang, H.; Li, D.; Tian, D.; Li, G.; Jing, X.; Zhang, W.; Xiao, W.; Liu, Q.; Zhang, F.; He, Z. Anomalously large interface charge in polarity-switchable photovoltaic devices: an indication of mobile ions in organic–inorganic halide perovskites. *Energy Environ. Sci.* **2015**, *8*, 1256-1260.